



Article

Comparative Analysis of Binhu and Cosmic-2 Radio Occultation Data

Hongjie Zhang ¹, Jingliang Huangfu ^{2,*}, Xingbao Wang ¹, Wen Chen ², Wenwu Peng ¹, Qi Tang ¹, Yiqi Chu ¹ and Ziyue Xue ¹

¹ Aerospace New Sky Technology Co., Ltd., Wuxi 214125, China

² Center for Monsoon System Research, Institute of Atmospheric Physics, Chinese Academy of Sciences, Beijing 100029, China

* Correspondence: hfjl@mail.iap.ac.cn

Abstract: Global Navigation Satellite System (GNSS) radio occultation (RO) technology has been widely used in Earth atmospheric detection and has a significant impact on numerical weather prediction (NWP), climate detection, and other fields. Cosmic-2 LEO-1 (C2E1) is a well-known RO data provider; however, its observations are confined to 45°S and 45°N. Recently, the Binhu meteorological observation test satellite (BH) has provided global coverage of RO data, including refractivity, specific humidity, and temperature data. In this study, RO data from BH and C2E1 are analyzed and compared from 8 February 2022 to 17 February 2022. Employing the European Centre for Medium-Range Weather Forecasts (ECMWF) reanalysis (ERA-5) data as a reference, both BH and C2E1 RO data agree with the ERA data, with the refractivity, temperature, and specific humidity profiles reflecting the real conditions of the natural atmosphere. In addition, BH data are comparable to C2E1 data at low and middle latitudes (0–45°), and BH data at middle and high latitudes (45–90°) are of better quality than those at low and middle latitudes (0–45°). For example, without considering the errors introduced by the interpolation of the ERA-5 data for comparative analysis, the BH refractivity profiles show a mean absolute bias of 0.73 N at low and middle latitudes and only 0.23 N at middle and high latitudes, and that for BH specific humidity profiles at middle and high latitudes is 0.015 g/kg, which is only half of that at low and middle latitudes. The BH temperature and specific humidity data show promising data accuracy. Therefore, BH RO data may provide important supplementary data at higher latitudes and may improve future NWP's through assimilation.

Keywords: GNSS; radio occultation; refractivity; specific humidity; temperature



Citation: Zhang, H.; Huangfu, J.; Wang, X.; Chen, W.; Peng, W.; Tang, Q.; Chu, Y.; Xue, Z. Comparative Analysis of Binhu and Cosmic-2 Radio Occultation Data. *Remote Sens.* **2022**, *14*, 4958. <https://doi.org/10.3390/rs14194958>

Academic Editor: Stefania Bonafoni

Received: 18 August 2022

Accepted: 30 September 2022

Published: 4 October 2022

Publisher's Note: MDPI stays neutral with regard to jurisdictional claims in published maps and institutional affiliations.



Copyright: © 2022 by the authors. Licensee MDPI, Basel, Switzerland. This article is an open access article distributed under the terms and conditions of the Creative Commons Attribution (CC BY) license (<https://creativecommons.org/licenses/by/4.0/>).

1. Introduction

Global Navigation Satellite System (GNSS) radio occultation (RO) technology is a nonconventional means to explore the Earth's atmosphere that integrates satellite remote sensing and navigation field detection methods. RO technology was originally used to probe planetary atmospheres in the 1960s [1–4], but it was not applied to probe the Earth's atmosphere until 1995 when the Global Positioning System (GPS)/Meteorology (MET) project was sponsored by the Center for Atmospheric Research, American University (UCAR) [5–7]. Their experimental results demonstrated that RO detection can provide temperature profiles with an accuracy of approximately 1 K. Thus, it has effectively promoted the development of GPS RO technology in atmospheric research. Since then, several GPS RO technology projects have been carried out worldwide, including the Challenging Mini-Satellite Payload (ChAMP), launched in 2000 [8]; the Constellation Observing System for Meteorology Ionosphere and Climate (COSMIC), launched in 2006 [9]; the FengYun-3C meteorological satellite, launched in 2013 [10] and the Meteorological Operational Polar Satellite series (MetOp-A, MetOp-B, and MetOp-C), launched in 2006, 2012, and 2018,

respectively [11,12]. At present, the GNSS has been further improved with Russia's Global Navigation Satellite System (GLONASS), the EU's Galileo satellite navigation system (GALILEO), and China's Beidou Navigation Satellite System (BDS), and the GNSS has entered the substantive operation stage. Thus, a revolutionary increase in the quantity of RO data has occurred.

RO probing theory has many advantages that conventional observation methods do not possess, such as global coverage, high vertical resolution, all-weather real-time observation, and long-term stability [13–15]. Some studies have confirmed that the RO profile has comparable accuracy to radiosonde data [16–18]. Thus, RO data have been widely used in numerical weather prediction (NWP). Many studies have shown that assimilating RO data can significantly improve the overall quality of NWP [11,19–22]. Luntama [11] found that since December 2006, the European Centre for Medium-Range Weather Forecasts (ECMWF) has begun to assimilate RO data, and the bias of ECMWF's forecast and analysis products has been significantly reduced, which indicates that RO data play an important role in the NWP. Subsequently, the National Centers for Environmental Prediction (NCEP) engaged in the operational study of RO data assimilation [23]. Liu and Xue [24] found significantly improved model results after assimilating Cosmic RO data. Bauer et al. [25] found that RO assimilation can significantly reduce the forecast errors in the Southern Hemisphere, while the reduction in the Northern Hemisphere and tropics was relatively small. This finding is related to the fact that the stations in the Northern Hemisphere are denser, and the acquired atmospheric data are much greater than those in the Southern Hemisphere. Therefore, RO data can fill the gap in observational data in the Southern Hemisphere, form encrypted observations for other regions, and improve the ability of the model background field to characterize the real atmosphere by data assimilation.

RO data have been widely used in forecast research on typhoons, rainstorms, and other high-impact weather phenomena. Many studies have shown that the assimilation of RO data has a positive effect on tropical cyclone tracks [26–31]. Mueller et al. [32] suggested that this is mainly attributed to the fact that RO detection can provide a large amount of atmospheric observation data at sea. Yang et al. [33] showed that RO data are conducive to the further study of tropical cyclone (TC) temperature and water vapor structures. Liu et al. [34] clearly showed that RO is also very helpful for studying TC genesis. Numerous studies have revealed that assimilated RO data can effectively improve the simulation of precipitation processes by global or regional models, thus improving the accuracy of precipitation forecasts [29,35,36]. In addition to contributing to the synoptic scale systems described above, RO data are also widely used in the field of climate. For example, Rao et al. [37] showed that RO data can be applied to the detection of the Indian summer monsoon outbreak, and Scherllin-Pirscher et al. [38] found that RO data can realize real-time monitoring of tropical temperature. In recent years, RO data have been applied to improve atmospheric river monitoring and simulations [39,40].

As the first satellite of the Linyun constellation program, the Binhu (BH) meteorological observation test satellite, which was independently developed by China, is equipped with a receiver to receive GNSS signals (including BDS, GALILEO, and GPS), and it was launched in October 2021. This satellite can effectively increase the global vertical profile data of atmospheric temperature, humidity, pressure, and other parameters and provide real-time data with high vertical resolution and high precision. Notably, some studies have found that the current NWP models are not saturated with the amount of assimilated RO data [25,41]. In other words, the higher the amount of assimilated occultation data is, the greater the contribution to the improvement of the current NWP. Thus, BH RO data can play an important role in improving the accuracy of NWP, and it is necessary to analyze BH data carefully to accelerate its application and development after a long, continuous period in which data are obtained.

The article is organized as follows. Section 2 provides a brief description of the different RO data and methods used. Section 3 describes the temporal characteristics of

different RO data. In Section 4, dry and wet atmospheric products of the BH and COSMIC-2 RO data are compared. Finally, Section 5 presents the conclusions of this study.

2. Data and Methods Descriptions

2.1. Data Description

The RO data used in this paper are the COSMIC-2 and BH RO Level-2 data products. The COSMIC-2 Level-2 data products are provided by the COSMIC Data Analysis and Archive Center (CDAAC), National Center for Atmospheric Research, the United States; BH RO Level-2 data products are provided by the Aerospace New Sky Meteorological Technology Co., Ltd., Wuxi, China. The Level-2 data products contain dry-atmosphere and wet-atmosphere data. The former contains the bending angle, refractivity, dry-atmosphere temperature, etc. The latter are obtained using the one-dimensional variational assimilation method, including wet atmospheric temperature and specific humidity, based on the former and the ERA Interim reanalysis data released by ECMWF. The 1-D assimilation variational method formulation is as follows:

$$J(x) = \frac{1}{2}(x - x_b)^T B^{-1}(x - x_b) + \frac{1}{2}(y - h(x))^T O^{-1}(y - h(x))$$

where $J(x)$ is the cost function, x is an atmospheric variable, x_b is the background field, y is a vector of the observations, B and O are the covariance matrices of background and observation error, respectively, and $h(x)$ is the observation operator. The data period is from 8 February 2022 to 17 February 2022. Since no model forecast contents are involved in this article, no additional quality control processing is performed on the data, except for the exclusion of profiles with refractivity values less than zero in the neutral atmosphere. In addition, due to the low top height of the currently used model, the RO data used for data assimilation are refractivity, so the main analysis work here focuses on the refractivity in the dry-atmosphere data and atmospheric temperature and specific humidity in wet-atmosphere data. Considering that the LY Constellation program is still in its early stages and has only one satellite at present, we use only Cosmic-2 LEO-1 (C2E1) satellite data for comparison.

The observation frequency of the sounding data is usually relatively low, with one observation conducted per day or per several hours. For the sounding data over land, we choose the ERA-5 reanalysis data as the observed “true value” for the comparative analysis of BH and Cosmic-2 data to assess the performance of the BH RO data. The hourly ERA-5 reanalysis data are provided by ECMWF with a horizontal resolution of $0.25^\circ \times 0.25^\circ$ and 37 levels in the vertical direction. The analysis time period for the ERA-5 reanalysis data is also consistent with the RO data.

2.2. Methods Description

Considering that the RO occurs at a relatively random time and position due to its detection mechanism, it is necessary to interpolate the gridded data to the observation locations in order to compare the BH and C2E1 RO data with ERA-5 reanalysis data. First, we conduct time matching for the ERA-5 reanalysis data and two kinds of RO data with a time interval of ± 0.5 h. Second, we conduct a linear interpolation of the ERA-5 reanalysis data time matching to the position where the RO direction occurs, i.e., interpolation from the grid point data to the irregularly distributed RO data in the horizontal direction, and then, we perform the conversion process from geopotential height to geometric height for the ERA-5 reanalysis data. The ERA-5 refractivity data can be calculated by the forward observation operator constructed from the temperature, pressure, and water vapor pressure. This observation operator is given following Smith [42]:

$$N = 77.6 \times \frac{P}{T} + 3.73 \times 10^5 \times \frac{e}{T^2}$$

where N is the refractivity (units: N), P is the pressure (units: hPa), T is the temperature (units: K), and e is the water vapor pressure (units: hPa). Finally, the above three data are interpolated to a uniform grid with a 0.2 km vertical resolution by using the cubic-spline algorithm. The drift of the tangential point is not taken into account during the RO data processing.

In addition, the bias, absolute bias, relative bias, and standard deviation (STD) of each variable are calculated as follows:

$$\sigma = X^{OBS} - X^{ERA}, \varepsilon = |\sigma|, \delta = \frac{\sigma}{X^{ERA}} \cdot 100\%, STD = \sqrt{\frac{1}{n-1} \sum_{i=1}^n \sigma^2}$$

where σ , ε , and δ are the bias, absolute bias, and relative bias, respectively; the superscripts "OBS" and ".ERA" indicate RO and ERA-5 data, respectively.

3. Temporal Characteristics of the RO Data

The BH and C2E1 data show some obvious differences in the observed location and minimum height of perigee points (Figures 1 and 2, respectively). Due to the large inclination of the BH satellite, the location of its observed RO data shows a global distribution and effectively improves the observation density at sea. Note that the minimum height of the BH profiles is higher than that of the C2E1 profiles, and it does not always show consistent characteristics as that in the C2E1 data (Figures 1 and 2). The reason for this is that the open-loop technique is only applied to GPS signal tracking until February 2022, which has been realized for BDS, GALILEO, and GPS signals recently. In contrast, since Cosmic-2 was initially established to monitor weather-scale systems in the tropics, especially tropical cyclones, they have a lower inclination, and the observation range is restricted to 45°S–45°N. Additionally, the formation of encrypted observations in the tropics through the constellation of six satellites shows increased received signal strength, enabling the observation of lower altitude atmospheric conditions. Therefore, the minimum height of the profiles observed by C2E1 behaves more consistently, mostly below 1 km. There is a small part of the data that has a minimum height above 4 km, but these data are mostly located near mountainous regions, such as the Tibetan Plateau (Figure 2b), so the minimum height of the observed profiles can be influenced by the elevation of the terrain. In addition to the differences in the spatial characteristics of BH and C2E1 RO data, there are also some differences in the number of observations. As shown in Figure 3a, the average number of daily observations of BH (C2E1) RO data is approximately 900 (1023), with a maximum of 963 (1077) and a minimum of 779 (981). Overall, the daily quantity of BH profiles is lower than that of C2E1 and the average number of Cosmic2 data (C2E1–C2E6) during the period from 8 February 2022 to 17 February 2022. The reason for the low number of BH data is that during this period, the BH satellite received only Beidou and GPS signals, but now it can receive Galileo signals, and approximately 1200 profiles can be obtained daily.

Until now, there was not a large difference in the number of profiles, but there have been some different characteristics in the minimum height of the perigee points of the profiles in each latitudinal region. In the BH data, the number of profiles with different minimum heights obviously varies at different latitudes (Figure 3b). For example, the absolute number of profiles with a minimum height greater than 6 km decreases with increasing latitude, the number of RO profiles with a minimum height of 2–4 km increases with increasing latitude, and those with a minimum height below 1 km are most abundant at latitudes of 15–75°. The characteristics of the minimum height of the C2E1 profiles are consistent in all latitudes, and the proportion of the data at each height does not change significantly, showing that the number of C2E1 data below 1 km is the highest, followed by 1–2 km and 2–4 km, while the proportion of data above 4 km is small (Figure 3c). Notably, compared to that of the COSMIC data, the COSMIC-2 data optimization is related to a high antenna gain [43] and signal-to-noise ratio (40 dB to 68 dB) [44], also higher than those

in the BH (antenna gain greater than 5 dBi and maximum signal-to-noise ratio of 40 dB to 48 dB).

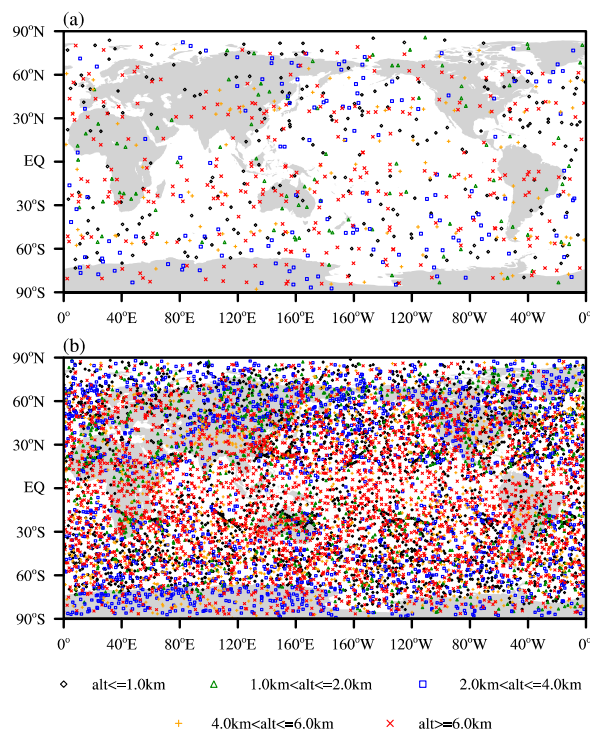


Figure 1. The characteristics of the spatial distribution for the BH RO observation location. (a) BH RO data on 20220208, (b) same as (a) but for the period of 8 February 2022 to 17 February 2022.

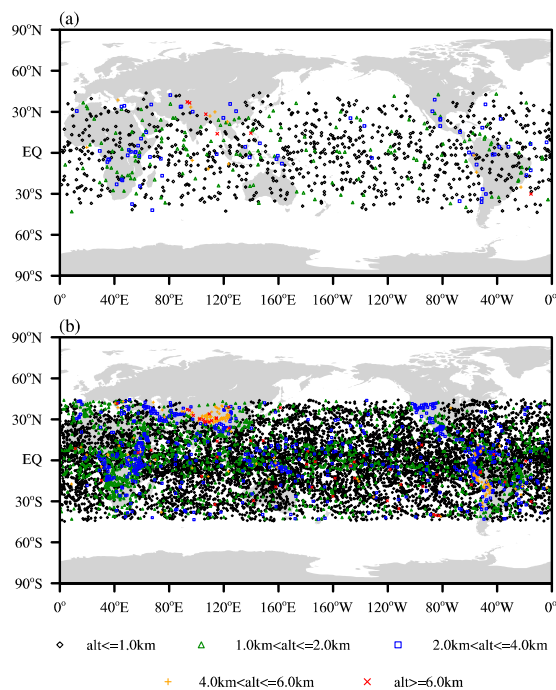


Figure 2. The characteristics of the spatial distribution for the C2E1 RO observation location. (a) C2E1 RO data on 20220208, (b) same as (a) but for the period of 8 February 2022 to 17 February 2022.

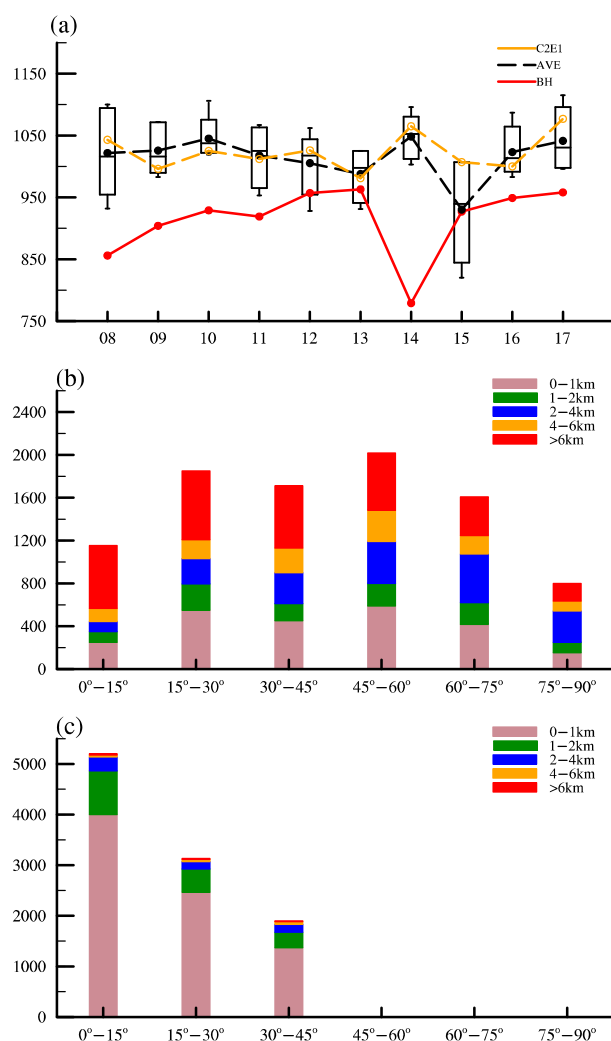


Figure 3. (a) Time series of the frequencies of the BH and C2E1 data; the frequencies of the (b) BH and (c) C2E1 data at different altitudes and latitudes.

4. Comparative Analysis

4.1. Refractivity Profile

The average refractivity profiles for different data (BH, C2E1, and ERA-5 data) have a consistent characteristic (Figure 4), which decreases and approaches 0 with increasing height, but they still have some differences in the range of values at different heights. At lower levels (0–10 km), the values of BH refractivity data lay within the range of ERA refractivity data; in contrast, the maximum and minimum values of C2E1 refractivity data are both smaller than those of the ERA-5. At higher levels (above 10 km), the maximum values of both BH and C2E1 refractivity data are greater than those of ERA-5 data, especially the latter (Figure 4a,b). Thus, it is necessary to analyze the differences between the BH (C2E1) data and the ERA-5 data in detail. From the perspective of the bias and STD of the data (Figure 5a–d), the mean refractivity profile of the BH and C2E1 data shows a negative bias below 2 km in the latitude range of 0–45°, 0–15°, 15–30°, and 30–45°, and the STD of the BH data is smaller than that of the C2E1 data. For these data, the bias is within -7 N and -12 N, respectively. These results indicate that the bias between the observations and reanalyzed data mainly originates from lower levels and lower latitudes. Within 2–20 km, the BH data have a positive bias with large STD, and the average value decreases obviously with increasing latitude. The maximum average bias is from 5.6 N to 1.2 N; at heights above 20 km, the BH data are close to 0. For C2E1 data, the bias is close to 0 from 2 km, and the STD is smaller than that of BH data below 10 km. In addition, the (absolute) bias and

STD of BH data outside the latitude of 45° are obviously smaller than that at latitudes of $0-45^\circ$, especially below 10 km (Figure 5d and Table 1).

Table 1. The average absolute bias and STD for BH and C2E1 RO data at latitudes of $0-45^\circ$ and $45-90^\circ$. The numbers in parentheses indicate STD values.

Data	Latitude	Refractivity (N)	Temperature (K)	Specific Humidity (g/kg)
BH	$0-45^\circ$	0.73 (1.43)	0.33 (1.52)	0.030 (0.15)
	$45-90^\circ$	0.23 (0.72)	0.41 (1.40)	0.015 (0.04)
C2E1	$0-45^\circ$	0.43 (1.12)	0.37 (1.10)	0.027 (0.13)

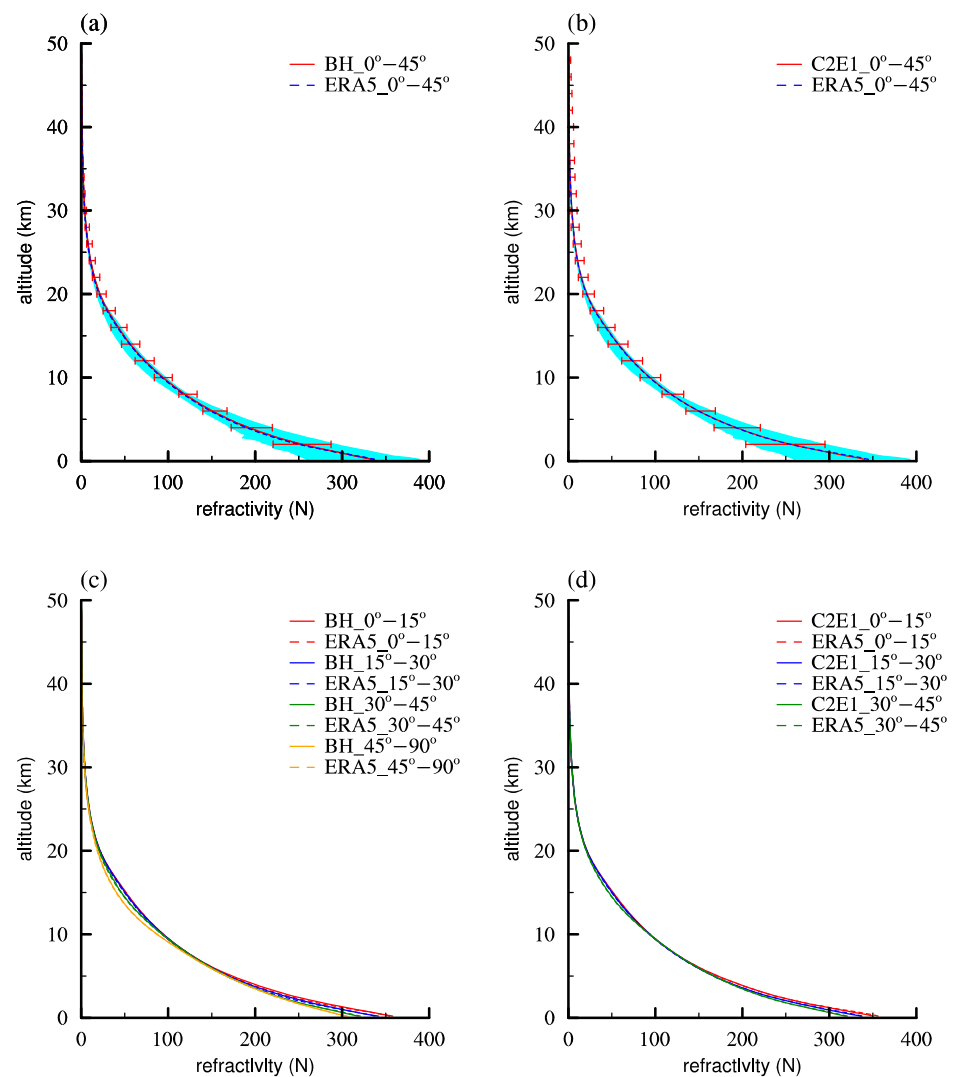


Figure 4. Vertical profiles of the average refractivity (units: N) for the BH, C2E1, and ERA-5 data at different latitudes. (a,c) BH and ERA-5 data; (b,d) C2E1 (red) and ERA-5 data. The bars indicate the range of BH (a) and C2E1 (b) refractivity values. Shadings in (a,b) indicate the range of ERA-5 refractivity values.

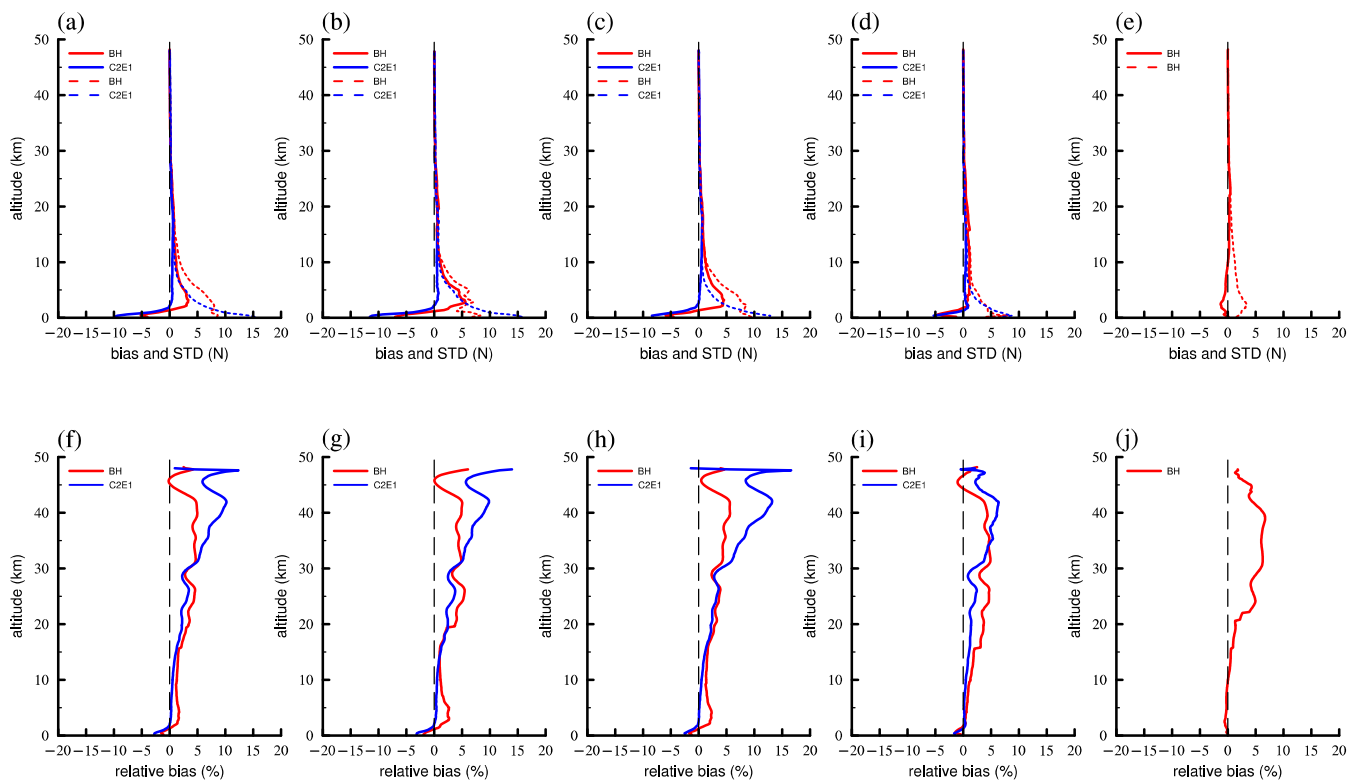


Figure 5. Vertical profiles of the average refractivity bias and STD (top; units: N) and (f–j) relative bias (bottom; units: %) for the BH and C2E1 data at different latitudes. (a–e) The average refractivity bias in the range of 0–45°, 0–15°, 15–30°, 30–45°, and 45–90°, respectively; (f–j) same as (a–e) but for the relative bias. The red and blue dashed lines indicate STD values of BH and C2E1, respectively.

The relative bias is used to further analyze the bias characteristics of the two types of RO data. As shown in Figure 5a, although the average relative bias for the refractivity profiles of BH and C2E1 data in the latitude range of 0–45° has a similar vertical structure, the magnitude of the refractivity bias exhibits some discrepancies. Specifically, in the latitude range of 0–15°, 15–30°, and 30–45°, the average relative bias for BH (C2E1) data in absolute terms is 1.57%, 1.72%, and 1.57% (0.94%, 0.88%, and 0.68%) below 20 km; 4.36%, 3.18%, and 3.87% (2.89%, 2.96%, and 1.61%) at 20–30 km; and 3.76%, 3.99%, and 3.31% (7.16%, 9.21%, and 4.39%) above 30 km, respectively. Thus, the refractivity bias of BH data is slightly larger than that of C2E1 data at lower altitudes, but that of BH data at high altitudes is much smaller in the different latitude ranges of 0–45°. Notably, the obvious fluctuation in the relative bias is related not only to the observation error of the RO detection itself and the error caused by data interpolation but also to the very small value of the refractivity caused by the thin air at a high level. Therefore, only a small amount of change in the refractivity at the top level can cause its relative bias to be magnified. Overall, the accuracies of the two types of RO refractivity data are comparable. In contrast with itself inside latitudes of 0–45°, the BH data outside latitudes of 0–45° have relative biases of 0.49%, 4.13%, and 5.27% at the corresponding latitudes, and the relative bias for BH outside latitudes of 45° is similar to that for C2E1 data inside latitudes of 0–45°.

Furthermore, the probability density function (PDF) of the relative bias between the refractivity of BH (C2E1) data shows that at 0–5 km (Figure 6a,b), most of the relative biases are kept within 5%. For BH data, the PDF with a relative bias greater than 5% is larger than C2E1, but this situation improves significantly with increasing latitude. As seen at 5–20 km (Figure 6b,c), there is a significant improvement in the data quality for both the BH and C2E1 data, and their PDFs are nearly symmetric and roughly fit the normal distribution. Even without quality control processing, the relative bias of most data at this height can be controlled within 2%. However, their PDFs shifted to the right at heights of 20–35 km and

above 35 km (Figure 7c,d,g,h), indicating that a more positive relative deviation appeared at high levels. The PDFs gradually flatten as the height increases, meaning that the number of large negative relative biases also increases gradually. This is also directly reflected in Figure 5f–j. In contrast, the BH refractivity data at middle and high latitudes are of better quality because their PDFs are nearly symmetric in the different ranges of altitudes, indicating that the overall data quality is closer to unbiased (Figure 5a–d).

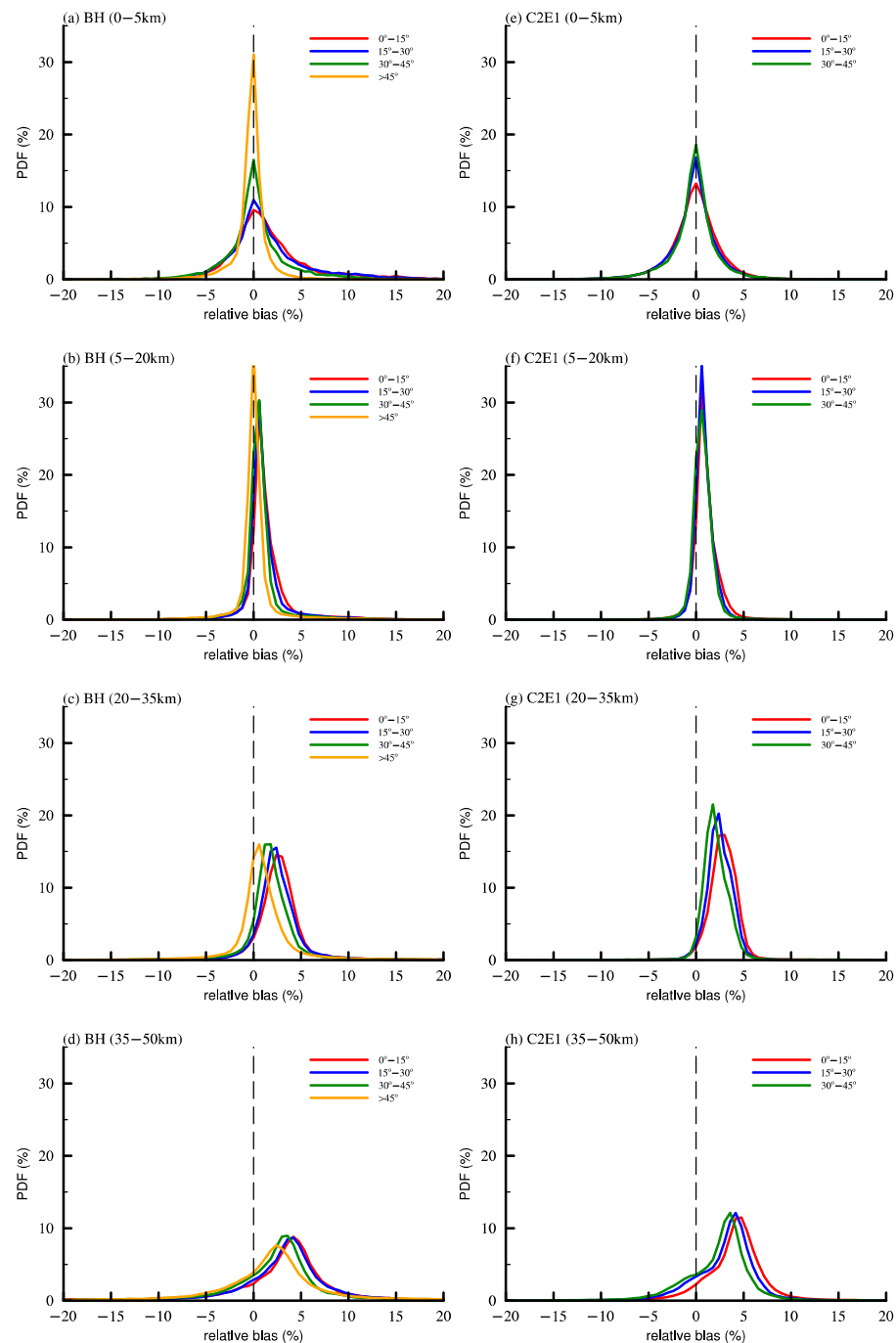


Figure 6. The probability density function (PDF) of the relative bias for BH and C2E1 at different heights. Refractivity data at different heights. (a–d) PDF for BH refractivity data at 0–5 km, 5–20 km, 20–35 km, and 35–50 km, respectively; (e–h) same as (a–d) but for C2E1 refractivity data. The red, orange, green, and blue lines indicate the mean relative bias of the refractivity in the latitude ranges of 0–15°, 15–30°, 30–45°, and 45–90°, respectively.

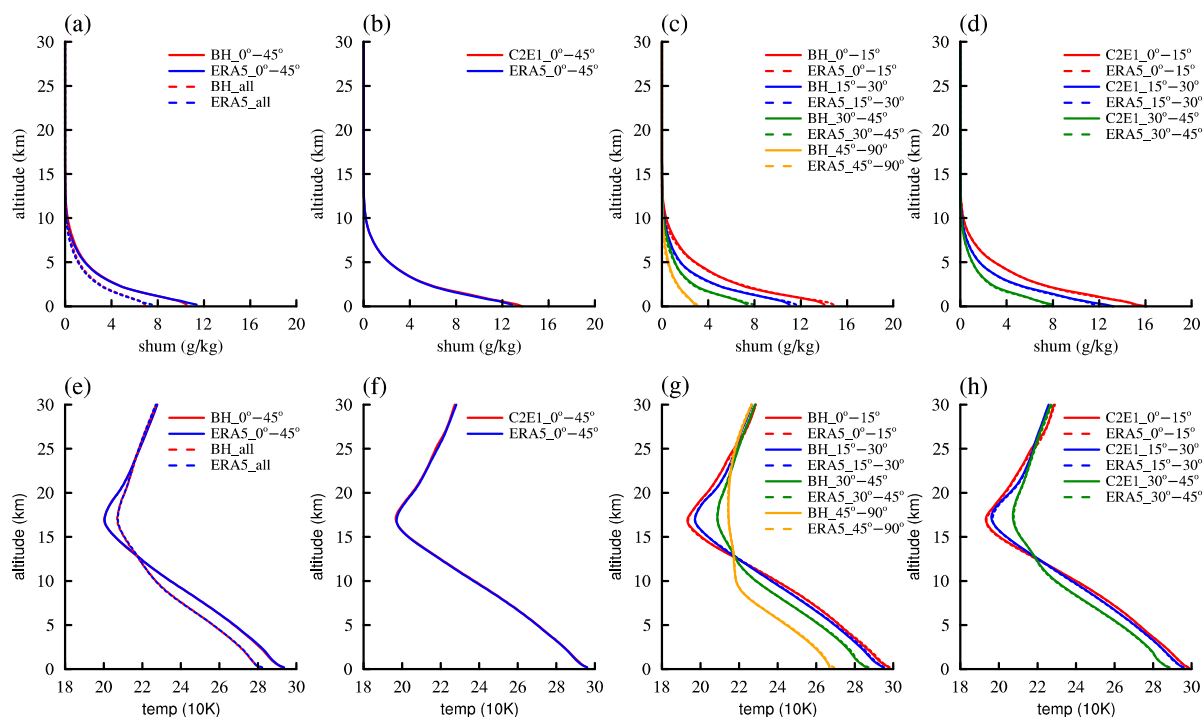


Figure 7. Vertical profiles of the average specific humidity (top; units: g/kg) and temperature (bottom; units: 10 K) for the BH, C2E1, and ERA-5 data at different latitudes. (a,c) BH and ERA-5 specific humidity data; (b,d) C2E1 (red) and ERA-5 specific humidity data; (e,g) BH and ERA-5 temperature data; (f,h) C2E1 (red) and ERA-5 temperature data.

In general, both BH and C2E1 data have good quality during the period of 8 February 2022 to 17 February 2022. The average (relative) biases of BH and C2E1 data in absolute terms are approximately 0.74 N (4.6%) and 0.80 N (4.7%), respectively. The STD values of BH and C2E1 data are 4.47 N and 2.12 N, respectively. That means that the average biases of BH data and C2E1 data are comparable, and the C2E1 data have a relatively smaller STD. Notably, the Cosmic-2 data are assimilated into the ERA-5 data, and they have some correlation with the ERA-5 data. Even so, the above statistics indicate that BH refractivity data in low- and middle-latitude regions (0–45°) perform comparably to C2E1, and BH data at middle and high latitudes (45–90°) are of better quality than those at low and middle latitudes.

4.2. Specific Humidity and Temperature Profile

This section mainly compares the specific humidity and temperature profiles of BH and C2E1 wet-atmosphere data, aiming to understand and analyze the characteristics of BH wet-atmosphere data. As shown in Figure 7a–d, the average profiles of specific humidity for BH and C2E1 data at different latitudes are very close to the mean value obtained from the ERA-5 data. Both data show that the abundant water vapor in the tropical troposphere (Figure 7c,d) and BH can exhibit relatively dry characteristics at middle and high latitudes, and the maximum of the average specific humidity is less than 4 g/kg (Figure 7c). Compared with the ERA data, the specific humidity of BH (C2E1) is smaller (larger) near the ground in Figure 7a,b. The temperature results in Figure 7e–h are similar to those in Figure 1 of Scherllin-Pirscher et al. [37], and the average profiles within the observation range and at different latitudes are consistent with the temperature profile values of the ERA data, while the characteristics of temperature decreased with increasing altitude in the troposphere and increased with increasing altitude in the stratosphere, reflecting the general pattern of temperature profile changes in the atmosphere. These results indicate that the BH data can accurately reflect the vertical distribution of water vapor and temperature in the natural atmosphere and have the ability to monitor atmospheric changes in real time.

In terms of the bias and STD of BH-specific humidity profiles (Figure 8a–d), the bias is relatively small below 2 km, within -0.72 g/kg, and the bias value decreases with increasing latitude. However, at 2–12 km, the relative bias of BH-specific humidity gradually increases with height, with a maximum average bias of approximately 0.17 g/kg. The average bias of the C2E1 specific humidity is similar to that of the BH data (Figure 8a–d), but the bias below 2 km is much larger, in which the main bias originates from the profile within 15° , and the maximum bias value can reach -1.0 g/kg. Although the bias is large at the bottom, it gradually approaches 0 g/kg above 2 km, and the maximum deviation does not exceed 0.16 g/kg. Both BH and C2E1 data have large STD below 10 km, where water vapor is plentiful, with the mean value of 0.50 g/kg and 0.44 g/kg. As shown in Figure 8e, the average bias of the BH-specific humidity profiles outside the latitude of 45° is within 0.015 g/kg, and the maximum value below 2 km is 0.08 g/kg, which is much smaller than that at other latitudes. In addition, the STD of the BH-specific humidity profiles outside the latitude of 45° at lower levels is also much smaller than in other latitudes, which indicates that the variation in the bias of the data is more stable. For all latitudes (Figure 8b–e), the biases of both specific humidity data above 12 km are close to 0, which is related to the scarcity of water vapor.

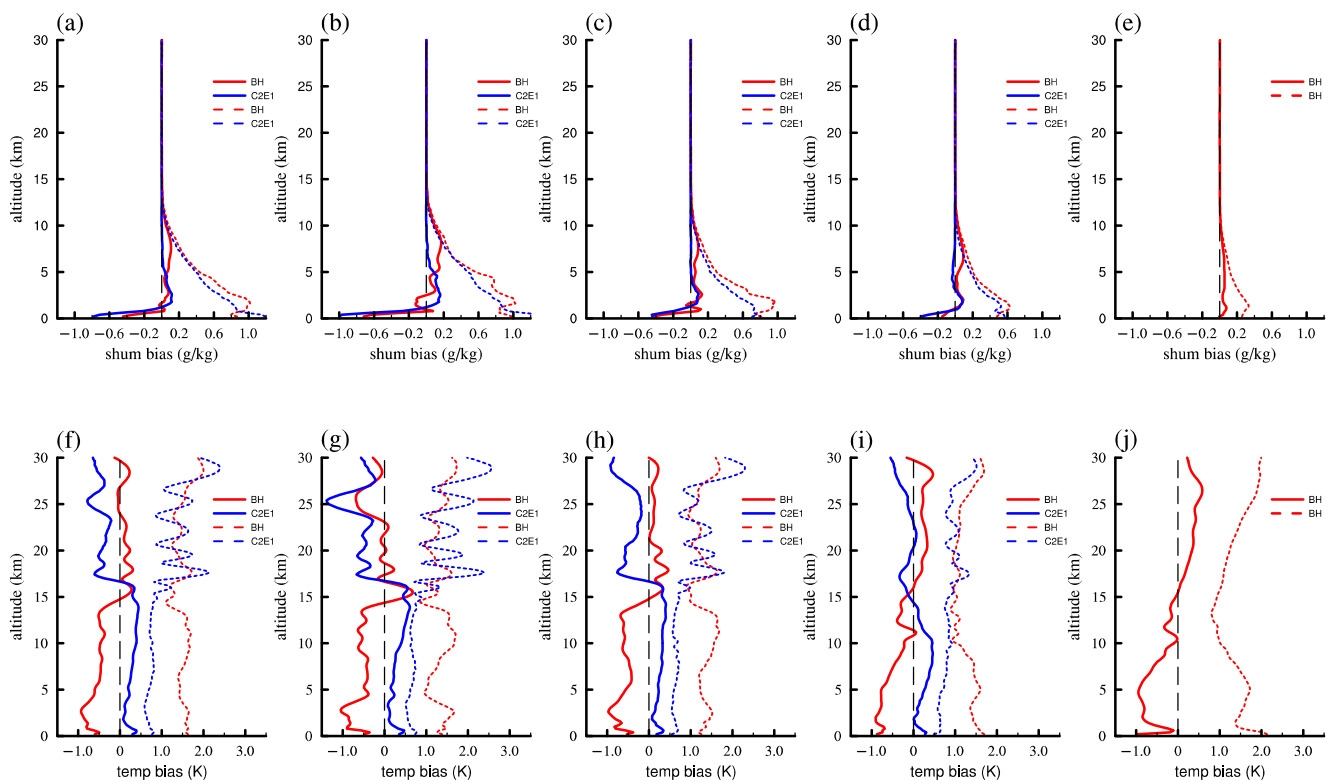


Figure 8. Vertical profiles of the average specific humidity bias, temperature and STD for the BH and C2E1 data at different latitudes. (a–e) The average specific humidity bias and STD (top; units: g/kg) in the range of $0\text{--}45^\circ$, $0\text{--}15^\circ$, $15\text{--}30^\circ$, $30\text{--}45^\circ$, and $45\text{--}90^\circ$, respectively; (f–j) same as (a–e) but for the temperature (bottom, units: K). The red and blue solid (dashed) lines indicate bias (STD) values of BH and C2E1 data, respectively.

From the bias and STD of the temperature profiles, it is interesting to note that the bias characteristics of the BH and C2E1 data are almost opposite (Figure 8f,g). The BH (C2E1) data have a mean negative (positive) bias of -0.53 k (0.29 K) at different latitudes below 15 km and decrease with height. In this altitude region, the STD of C2E1 (0.73 K) is much smaller than that of BH (1.52 K). In the range of $15\text{--}30$ km, the BH (C2E1) data have a positive (negative) bias, with a mean value of 0.11 K (-0.38 k), and the STD values of BH and C2E1 data are comparable, with a mean value of 1.52 K and 1.46 K. Therefore, in this

height range, the BH data perform better. The average bias and STD of the BH temperature profiles outside the latitude of 45° are shown in Figure 8j. Although the bias below 15 km is similar to that at other latitudes, which is -0.48 K, the bias at 15–30 km is greater than that at other latitudes, which is 0.33 K, and the STD is larger than that of other latitudes.

Overall, the average absolute bias of the BH (C2E1) specific humidity data is 0.030 g/kg (0.027 g/kg), and that of the BH (C2E1) temperature data is 0.33 K (0.37 K). Thus, BH data can provide specific humidity and temperature profiles with comparable accuracy to the C2E1 data. The average absolute bias of the BH-specific humidity data over a latitude of 45° is 0.015 g/kg, which is less than that within a latitude of 45° , and for the BH temperature data, the average absolute bias is 0.41 K, which is comparable to that within the latitude of 45° (Table 1). Considering that the BH and C2E1 RO wet-atmosphere data are obtained based on the retrieval products of ERA-5 and NCEP reanalysis data, respectively, the reasons for the differences in their bias characteristics need to be analyzed in depth in the future.

5. Conclusions

During the period of 08–17 February 2022, RO data acquired by the BH satellite showed global distribution characteristics. The BH satellite has observed more than 900 profiles every day before opening the channel to receive Galileo signals. Most of the minimum height at the BH data perigee is above 2 km, but due to the enhanced receiving antenna, most profiles of the C2E1 data can acquire atmospheric states below 1 km.

For dry-atmosphere refractivity data in low- and middle-latitude regions (0 – 45°), compared with the ERA-5 data, the overall detection accuracy of the BH data and C2E1 data is quite close, with average relative biases in absolute terms of approximately 2.3% and 2.5%, respectively. The former has better data quality at higher levels, while the latter has better data quality at lower levels. Notably, the BH data at middle and high latitudes (45 – 90°) are of better quality than those at low and middle latitudes.

For wet-atmosphere temperature and specific humidity data, the mean profiles of temperature and humidity are consistent with the ERA-5 data. This finding shows that the two data products can accurately reflect the real conditions of the temperature and humidity of the atmosphere. Further analysis reveals that in the low troposphere, the average bias of the BH (C2E1) specific humidity profiles is smaller (larger). However, as the height increases, there is an increase in the bias of the BH-specific humidity, with a maximum average bias reaching 0.1 g/kg, while the bias of C2E1 is close to 0. This finding indicates that the accuracy of the BH-specific humidity data needs further improvement. For the temperature profiles, the two kinds of data have nearly opposite bias characteristics. Below 15 km, the bias of the BH temperature is negative (-0.53 K), and that of the C2E1 data is positive (0.29 K); at 15–30 km, the bias of BH is positive (0.11 K), and that of the C2E1 data is negative (-0.38 K).

As a result, the BH data provide accuracies comparable to that of C2E1 at latitudes of 0 – 45° , including the refractivity, temperature, and specific humidity profiles. In addition, the overall performance of the refractivity and specific humidity data at latitudes of 45 – 90° is better than that at latitudes of 0 – 45° . The accuracy of the BH temperature data below 15 at latitudes of 45 – 90° is similar to that at latitudes of 0 – 45° . Therefore, BH provides important supplementary data at higher latitudes and forms an effective complementary relationship with C2E1 data.

Notably, the vertical resolution of the ERA-5 data is much lower than that of the RO data, so the interpolation method would inevitably cause a difference. In addition, the current data are not long enough to conduct a climatological analysis of RO data. Based on future observation and statistical analysis, our work will keep improving the quality of the BH data.

Author Contributions: Conceptualization, H.Z. and J.H.; methodology, H.Z.; software, H.Z.; validation, H.Z., J.H. and X.W.; data curation, H.Z. and X.W.; writing—original draft preparation, H.Z., J.H, W.P., Q.T., Y.C. and Z.X. supervision, X.W. and W.C. All authors have read and agreed to the published version of the manuscript.

Funding: This research was funded by the National Natural Science Foundation of China (41721004), the State Key Laboratory of Tropical Oceanography (South China Sea Institute of Oceanology Chinese Academy of Sciences) (Grant LTO2104), and the Key Program of the Chinese Academy of Sciences (Grant QYZDY-SSW-DQC024).

Data Availability Statement: The Comsic-2 and ERA-5 data support the findings of this study and are available at <https://cdaac-www.cosmic.ucar.edu>, date of citation: 18 April 2022 and <https://www.ecmwf.int/en/forecasts/dataset/ecmwf-reanalysis-v5>, date of citation: 6 April 2022.

Acknowledgments: We thank the CDAAC, Aerospace New Sky Technology Co., Ltd. and ECMWF for the RO data and ERA-5 data. The authors are grateful for the comments and suggestions provided by the editor and anonymous reviewers.

Conflicts of Interest: The first, third, fifth, sixth, and seventh authors of the present study are employed by New Sky Technology Co., which has been committed to developing RO data based on its own satellite observations. The authors declare that there are no conflicts of interest: we ensure that our research is appropriately and objectively in accordance with scientific guidelines and reports when there are actual or potential conflicts with competing companies.

References

- Kliore, A.; Cain, D.L.; Levy, G.S.; Eshleman, V.R.; Fjeldbo, G.; Drake, F.D. Occultation experiment: Results of the first direct measurement of Mars's atmosphere and ionosphere. *Science* **1965**, *149*, 1243–1248. [[CrossRef](#)]
- Fjeldbo, G.; Eshleman, V.R. The atmosphere of Mars analyzed by integral inversion of the Mariner IV occultation data. *Planet. Space Sci.* **1968**, *16*, 1035–1059. [[CrossRef](#)]
- Eshleman, V.R. The radio occultation method for the study of planetary atmospheres. *Planet. Space Sci.* **1973**, *21*, 1521–1531. [[CrossRef](#)]
- Yunck, T.P. An overview of atmospheric radio occultation. *J. Glob. Posit. Syst.* **2002**, *1*, 58–60. [[CrossRef](#)]
- Ware, R.; Rocken, C.; Solheim, F.; Exner, M.; Kuo, Y.H. GPS sounding of the atmosphere from low Earth orbit: Preliminary results. *Bull. Am. Meteorol. Soc.* **1996**, *77*, 19–40. [[CrossRef](#)]
- Kursinski, E.R.; Hajj, G.A.; Bertiger, W.I.; Leroy, S.S.; Meehan, T.K.; Romans, L.J.; Schofield, J.T.; McCleese, D.J.; Melbourne, W.G.; Thornton, C.L. Initial results of radio occultation observations of Earth's atmosphere using the Global Positioning System. *Science* **1996**, *271*, 1107–1110. [[CrossRef](#)]
- Feng, D.D.; Herman, B.M. Remotely Sensing the Earth's Atmosphere Using the Global Positioning System (GPS)—The GPS/MET Data Analysis. *J. Atmos. Ocean. Technol.* **1999**, *16*, 989–1002. [[CrossRef](#)]
- Wickert, J.; Reigber, C.; Beyerle, G.; Knig, R.; Hocke, K. Atmosphere sounding by GPS radio occultation: First results from CHAMP. *Geophys. Res. Lett.* **2001**, *28*, 3263–3266. [[CrossRef](#)]
- Anthes, R.A.; Ector, D.; Hunt, D.C.; Kuo, Y.H.; Rocken, C.; Schreiner, W.S.; Syndergaard, S.; Wee, T.K.; Zeng, Z. The COSMIC/FORMOSAT-3 mission: Early results. *Bull. Am. Meteorol. Soc.* **2012**, *89*, 313–333. [[CrossRef](#)]
- Tian, M.; Sun, L.; Yang, G.; Yue, X.; Tao, Y.; Cong, H.; Zeng, Z.; Wang, Y.; Wang, J. First Ionospheric Radio-Occultation Measurements From GNSS Occultation Sounder on the Chinese Feng-Yun 3C Satellite. *IEEE T. Geosci. Remote* **2016**, *54*, 5044–5053.
- Luntama, J.P.; Kirchengast, G.; Borsche, M.; Foelsche, U.; Marquardt, C. Prospects of the EPS GRAS mission for operational atmospheric applications. *Bull. Am. Meteorol. Soc.* **2008**, *89*, 1863–1875. [[CrossRef](#)]
- Edwards, P.G.; Berutti, B.; Blythe, P.; Callies, J.; Franssen, C.; Kruttsch, R.; Lefebvre, A.R.; Loiselet, M.; Stricker, N. The MetOp satellite-Weather information from polar orbit. *ESA Bull.* **2006**, *127*, 8–17.
- Kursinski, E.R.; Hajj, G.A.; Schofield, J.T.; Linfield, R.P.; Hardy, K.R. Observing earth's atmosphere with radio occultation measurements using the global positioning system. *J. Geophys. Res. Atmos.* **1997**, *102*, 23429–23465. [[CrossRef](#)]
- Healy, S.B. Smoothing radio occultation bending angles above 40 km. *Ann. Geophys.* **2001**, *19*, 459–468. [[CrossRef](#)]
- Hajj, G.A.; Kursinski, E.R.; Romans, L.J.; Bertiger, W.I.; Leroy, S.S. A technical description of atmospheric sounding by GPS occultation. *J. Atmos. Sol.-Terr. Phys.* **2002**, *64*, 451–469. [[CrossRef](#)]
- Fu, E.J.; Zhang, K.F.; Marion, K.Y.; Xu, X.H.; Marshall, J.; Rea, A.; Weymouth, G.; Kuleshov, Y. Assessing COSMIC GPS radio occultation derived atmospheric parameters using Australian radiosonde network data. *Procedia Earth Planet. Sci.* **2009**, *1*, 1054–1059. [[CrossRef](#)]
- He, W.; Ho, S.P.; Chen, H.; Zhou, X.; Hunt, D.; Kuo, Y.H. Assessment of radiosonde temperature measurements in the upper troposphere and lower stratosphere using COSMIC radio occultation data. *Geophys. Res. Lett.* **2009**, *36*, L17807. [[CrossRef](#)]

18. Sun, B.; Reale, A.; Seidel, D.J.; Hunt, D.C. Comparing radiosonde and COSMIC atmospheric profile data to quantify differences among radiosonde types and the effects of imperfect collocation on comparison statistics. *J. Geophys. Res. Atmos.* **2010**, *115*, 1–16. [[CrossRef](#)]
19. Hatanaka, Y.; Mannoji, N.; Naito, I.; Ichikawa, R.; Shimada, S.; Yabuki, T.; Tsuji, H.; Tanaka, T. Global positioning system project to improve Japanese weather, earthquake predictions. *EOS Trans. Am. Geophys. Union* **1998**, *79*, 301–311.
20. Healy, S.B. Forecast impact experiment with a constellation of GPS radio occultation receivers. *Atmos. Sci. Lett.* **2008**, *9*, 111–118. [[CrossRef](#)]
21. Poli, P.; Moll, P.; Puech, D.; Rabier, F.; Healy, S.B. Quality control, error analysis, and impact assessment of FORMOSAT3/COSMIC in numerical weather prediction. *Terr. Atmos. Ocean. Sci.* **2009**, *20*, 101–113. [[CrossRef](#)]
22. Rennie, M.P. The impact of GPS radio occultation assimilation at the Met Office. *Q. J. Roy. Meteor. Soc.* **2010**, *136*, 116–131. [[CrossRef](#)]
23. Cucurull, L. Assimilation of Global Positioning System Radio Occultation Observations into NCEP's Global Data Assimilation System. *Mon. Wea. Rev.* **2010**, *135*, 3174–3193. [[CrossRef](#)]
24. Liu, Y.; Xue, J. Assimilation of GNSS radio occultation observations in GRAPES. *Atmos. Meas. Tech.* **2014**, *7*, 7613–7639. [[CrossRef](#)]
25. Bauer, P.; Radnóti, G.; Healy, S.; Cardinali, C. GNSS Radio Occultation Constellation Observing System Experiments. *Mon. Wea. Rev.* **2014**, *142*, 555–572. [[CrossRef](#)]
26. Chen, S.Y.; Huang, C.Y.; Kuo, Y.H.; Guo, R.Y.; Sokolovskiy, S. Assimilation of GPS refractivity from FORMOSAT3/COSMIC using a nonlocal operator with WRF 3DVAR and its impact on the prediction of a typhoon event. *Terr. Atmos. Ocean. Sci.* **2009**, *20*, 133–154. [[CrossRef](#)]
27. Ma, Z.; Kuo, Y.H.; Wang, B.; Wu, W.S.; Sokolovskiy, S. Comparison of local and nonlocal observation operators for the assimilation of GPS RO data with the NCEP GSI system: An OSSE study. *Mon. Wea. Rev.* **2009**, *137*, 3575–3587. [[CrossRef](#)]
28. Kueh, M.T.; Huang, C.Y.; Chen, S.Y.; Chen, S.H.; Wang, C.J. Impact of GPS Radio Occultation Refractivity Soundings on a Simulation of Typhoon Bilis (2006) Upon Landfall. *Terr. Atmos. Ocean. Sci.* **2009**, *20*, 115–131. [[CrossRef](#)]
29. Huang, C.Y.; Kuo, Y.H.; Chen, S.Y.; Terng, C.T.; Chien, F.C.; Lin, P.L.; Kueh, M.T.; Chen, S.H.; Yang, M.J.; Wang, C.J.; et al. Impact of GPS radio occultation data assimilation on regional weather predictions. *GPS Solut.* **2010**, *14*, 35–49. [[CrossRef](#)]
30. Kunii, M.; Seko, H.; Ueno, M. Impact of Assimilation of GPS Radio Occultation Refractivity on the Forecast of Typhoon Usagi in 2007. *J. Meteor. Soc. Jpn.* **2012**, *90*, 255–273. [[CrossRef](#)]
31. Chen, Y.C.; Hsieh, M.E.; Hsiao, L.F.; Kuo, Y.H.; Yang, M.J.; Huang, C.Y.; Lee, C.S. Systematic evaluation of the impacts of GPSRO data on the prediction of typhoons over the northwestern Pacific in 2008–2010. *Atmos. Meas. Tech. Discuss.* **2015**, *8*, 2531–2542. [[CrossRef](#)]
32. Mueller, M.J.; Kren, A.C.; Cucurull, L.; Casey, S.P.F.; Peevey, T.R. Impact of refractivity profiles from a proposed GNSS-RO constellation on tropical cyclone forecasts in a global modeling system. *Mon. Wea. Rev.* **2020**, *148*, 3037–3057. [[CrossRef](#)]
33. Yang, S.; Zou, X.; Ray, P.S. Comparison of TC temperature and water vapor climatologies between the Atlantic and Pacific Oceans from GPS RO observations. *J. Climate* **2018**, *31*, 8557–8571. [[CrossRef](#)]
34. Liu, H.; Anderson, J.E.; Kuo, Y.H. Improved Analyses and Forecasts of Hurricane Ernesto's Genesis Using Radio Occultation Data in an Ensemble Filter Assimilation System. *Mon. Wea. Rev.* **2012**, *140*, 151–166. [[CrossRef](#)]
35. Huang, C.Y.; Kuo, Y.H.; Rao, A.; Chen, S.Y. The assimilation of GPS radio occultation data and its impact on rainfall prediction along the west coast of India during monsoon 2002. *Pure Appl. Geophys.* **2007**, *164*, 1577–1591. [[CrossRef](#)]
36. Yang, S.C.; Chen, S.H.; Chen, S.Y.; Huang, C.Y.; Chen, C.S. Evaluating the impact of the COSMIC RO bending angle data on predicting the heavy precipitation episode on 16 June 2008 during SoWMEX-IOP8. *Mon. Wea. Rev.* **2014**, *142*, 4139–4163. [[CrossRef](#)]
37. Rao, V.V.M.J.; Ratnam, M.V.; Santhi, Y.D.; Raman, M.R.; Rao, S.V.B. On the detection of onset and activity of the Indian summer monsoon using GPS RO refractivity profiles. *Mon. Wea. Rev.* **2013**, *141*, 2096–2106. [[CrossRef](#)]
38. Scherllin-Pirscher, B.; Steiner, A.K.; Anthes, R.A.; Alexander, A.J.; Zeng, Z. Tropical Temperature Variability in the UTLS: New Insights from GPS Radio Occultation Observations. *J. Climate* **2020**, *34*, 2813–2838. [[CrossRef](#)]
39. Neiman, P.J.; Ralph, F.M.; Wick, G.A.; Kuo, Y.H.; Wee, T.K.; Ma, Z.; Taylor, G.H.; Dettinger, M.D. Diagnosis of an intense atmospheric river impacting the Pacific Northwest: Storm summary and offshore vertical structure observed with COSMIC satellite retrievals. *Mon. Wea. Rev.* **2008**, *136*, 4398–4420. [[CrossRef](#)]
40. Guo, X.; Zhao, N.; Kikuchi, K.; Nasuno, T.; Nakano, M.; Annamalai, H. Atmospheric Rivers over the Indo-Pacific and Its Associations with the Boreal Summer Intraseasonal Oscillation. *J. Climate* **2021**, *34*, 9711–9728.
41. Harnisch, F.; Healy, S.B.; Bauer, P.; English, S.J. Scaling of GNSS Radio Occultation Impact with Observation Number Using an Ensemble of Data Assimilations. *Mon. Wea. Rev.* **2013**, *141*, 4395–4413. [[CrossRef](#)]
42. Smith, E.K.; Weintraub, S. The constants in the equation for atmospheric refractive index at radio frequencies. *Proc. IRE* **1953**, *41*, 1035–1037. [[CrossRef](#)]
43. Cucurull, L.; Casey, S.P.F. Improved Impacts in Observing System Simulation Experiments of Radio Occultation Observations as a Result of Model and Data Assimilation Changes. *Mon. Wea. Rev.* **2021**, *149*, 207–220. [[CrossRef](#)]
44. Schreiner, W.S.; Weiss, J.P.; Anthes, R.A.; Braun, J.; Chu, V.; Fong, J.; Hunt, D.; Kuo, Y.-H.; Meehan, T.; Serafino, W.; et al. COSMIC-2 Radio Occultation Constellation-First Results. *Geophys. Res. Lett.* **2020**, *47*, e2019GL086841. [[CrossRef](#)]